International Core Journal of Engineering Volume 12 Issue 5, 2026
ISSN: 2414-1895 DOI: 10.6919/ICJE.202605_12(5).0014

Microstructure and High-temperature Friction Wear Properties of Laser-cladded $Fe_{20}Co_{20}Cr_{20}Ni_{25}Al_xTi_{(15-x)}$ High-entropy Alloy Coatings

Yarong Chen*, Xiong Yang, Yaoguang Wei, Qiaoling Wang, Yue Yan, Guangqi Ran, Guangpei Xu, Sainan Chen, Shimei Tao, Yifan Zhang, Ting Wen

Chengdu Aircraft Industrial (Group) Co., Ltd., Chengdu 610092, China

Abstract

High-speed train brake discs at 400 km/h are coated with $Fe_{20}Co_{20}Cr_{20}Ni_{25}Al_xTi_{(15-x)}$ high-entropy alloy to improve the service performance of the discs and ensure train safety. In this study, $Fe_{20}Co_{20}Cr_{20}Ni_{25}Al_xTi_{(15-x)}$ high-entropy alloy coating was successfully prepared on 24CrNiMo, a steel-based material for brake discs, and its microstructure and hardness, high-temperature frictional wear properties, and mechanism were investigated. It was discovered that the phase structure of the $Fe_{20}Co_{20}Cr_{20}Ni_{25}Al_xTi_{(15-x)}$ high-entropy alloy cladding layer is the face-centered cubic phase, and the microstructure of the clad layer is flat crystal, columnar crystal, dendritic crystal and equiaxed crystal from the bottom to the top in order. The average friction coefficient of $Fe_{20}Co_{20}Cr_{20}Ni_{25}Al_xTi_{(15-x)}$ high-entropy alloy is between 0.3 and 0.6, which is lower than that of the substrate. The room temperature and high-temperature wear rates of $Fe_{20}Co_{20}Cr_{20}Ni_{25}Al_5Ti_{10}$ were reduced by 51.1% and 74.2%, respectively, compared to the substrate, with enhanced wear performance. The room-temperature wear mechanism of $Fe_{20}Co_{20}Cr_{20}Ni_{25}Al_xTi_{(15-x)}$ was all abrasive wear, and the high-temperature wear mechanisms were oxidation wear, adhesive wear and abrasive wear.

Keywords

High-speed Train Brake Disc; Laser Cladding; High-entropy Alloy; High-temperature Friction Wear.

1. Introduction

Currently, high-speed trains have developed to 400 km/h [[1],[2]]. As the train speed increases, the requirements for the braking system, encompassing both braking technology and safety, become more stringent. Research indicates that the brake energy heat load on the surface of the brake disc of high-speed trains above 400 km/h can reach more than 800 ℃ [[3]]. Yet the existing cast steel brake disc with poor high-temperature resistance at 400 km/h for a long time in service will induce thermal wear or thermal fatigue failure on the brake disc surface or near the surface, resulting in a shortened service life of the train [[4],[5]]. Therefore, the fabrication of wear-resistant reinforcement material on the surface of brake discs to improve the performance of train brake discs has become a hot research topic in the past decade [[6]-[9]].

The research focuses on the surface modification of cast steel brake discs using existing powder material systems (such as iron-based alloys is insufficient, the matching between nickel-based alloys and copper-based brake pads is poor, and the thermal fatigue resistanc of cobalt-based alloys is still relatively poor compared to brake discs materials. In 2004, Taiwanese scholars Junwei Yeh [[10]] and Cantor B [[11]] et al. of Oxford University proposed a design model with multiple major elements as the basic building blocks of high entropy alloys (HEAs). HEAs have a unique crystal structure,

ISSN: 2414-1895 DOI: 10.6919/ICJE.202605_12(5).0014

which contributes to their excellent wear resistance [[12],[13]], thermal stability [[14],[15]], and high-temperature oxidation resistance [[16]]. Statistics obtained transition group elements Fe, Co, Cr and Ni appear in many choices of high entropy alloy material systems respectively, and their excellent properties are approved by most scholars [[17]]. Investigation found that the addition of Si, Al, Mo, Ti and other elements with large differences in atomic size from Fe, Co, Cr, Ni, etc., the hardness and strength of high-entropy alloys increase, and their strengthening mechanisms are generally solid solution strengthening or precipitation strengthening or mixed mechanisms of solid solution strengthening and precipitation strengthening. The room temperature strength of high entropy alloys is excellent, but the specific strengths of general high entropy alloys are significantly reduced above 600 °C [[18]]. The simultaneous addition of Al and Ti elements decreases the degree of strength reduction and produces the best specific strength values comparable to those of high-performance steels and polycrystalline high-temperature alloys [[19]-[22]]. In general, the addition of Al and Ti elements to the FeCoCrNi system is beneficial to enhance the basic mechanical properties at room temperature and high-temperature oxidation resistance of the high-entropy alloy in this system [[23],[24]].

It was found that thermal spraying cannot avoid oxygen and carbon contamination, which seriously reduces the performance [[25]]; magnetron sputtering has difficulty in manufacturing a coating with a specified thickness and low material utilization [[26]]; laser cladding has the advantages of the small heat-affected zone, low dilution rate and high bond strength and can form a coating with a certain thickness, so it is widely used [[27],[28]].

This study aims to solve the lack of high-temperature wear resistance of cast steel brake disc 24CrNiMo steel for 400 km/h and uses laser cladding to prepare high-performance high-entropy alloy coatings on the surface of the brake disc to improve the high-temperature performance.

2. Materials and Methods

2.1 Sample Preparation

In this study, the substrate used is cast steel 24CrNiMo for high-speed train brake discs, which has a size of 100 mm ×100 mm ×8 mm.The surface is polished smooth and bright with a sander first, and then washed with alcohol to remove impurities. Table 1 and Figure 1 show respectively the composition content and microstructure of 24CrNiMo. The high-entropy alloy powder was chosen as $Fe_{20}Co_{20}Cr_{20}Ni_{25}Al_xTi_{(15-x)}$ (x=0,5,10,15), where x is the atomic ratio of Al elements added. For subsequent convenience, the coated HEAs are briefly written as Al_0Ti_{15}, Al_5Ti_{10}, $Al_{10}Ti_5$, and $Al_{15}Ti_0$, respectively. Fe, Co, Cr, Ni, Al and Ti all powders were spherical, but the irregular shape still existed. The powders were purchased from Changsha Tianjiu Metal Materials, and the specific mass fractions are shown in Table 1.

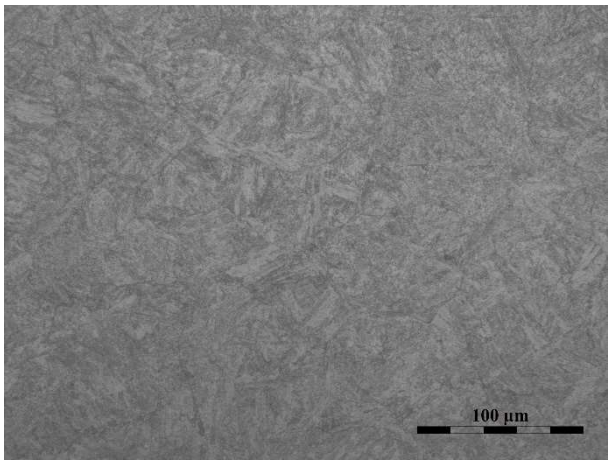

Figure 1. Microstructure of 24CrNiMo.

ISSN: 2414-1895 DOI: 10.6919/ICJE.202605_12(5).0014

Table 1. Composition content of 24CrNiMo (wt.%).

Element	Fe	C	Si	Cr	Ni	Mo	P	S
24CrNiMo	Bal.	0.23	0.27	0.70	0.45	0.25	0.028	0.032

Table 2. Mass fraction of each element of high entropy alloy powder (wt.%).

Sample	Fe	Co	Cr	Ni	Al	Ti
Al_0Ti_{15}	20.231	21.348	18.836	26.577	0	13.008
Al_5Ti_{10}	20.621	21.760	19.199	27.090	2.491	8.840
$Al_{10}Ti_5$	21.026	22.188	19.577	27.622	5.079	4.507
$Al_{15}Ti_0$	21.448	22.633	19.969	28.177	7.772	0

According to the ball material ratio of 10:1, it is mixed in the YXQM-2L planetary ball mill at 100 r/min for 8 hours. Whereafter, the mixed powders were dried in a vacuum drying oven at 100 °C for 2 h. The scanning electron microscope images of the high entropy alloy powders are shown in Figure 2, which indicates that the added elements were mixed well.

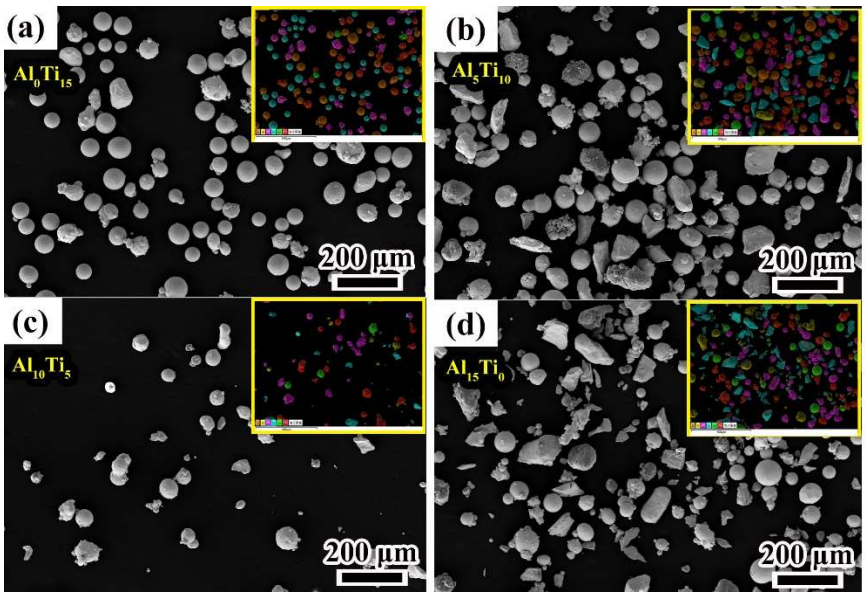

Figure 2. SEM morphology of the mixed high entropy alloy powder. (a)Al_0Ti_{15}; (b)Al_5Ti_{10}; (c)$Al_{10}Ti_5$; (d)$Al_{15}Ti_0$.

RFL-C6000 laser cladding system equipped with a 6.0 kW solid-state laser with fiber transmission and a coaxial laser head with a lens focal length of 300 mm and a laser wavelength of 1064 nm, the equipment schematic diagram is shown in Figure 3. Argon was used as the powder carrier, high-purity argon (99.999%) was used as the protective gas, the spot diameter was 3 mm, the carrier gas volume was 7 L/min, the protective gas flow rate are 50L/min and the lap rates were all 40%. The laser deposition process parameters were optimized according to the orthogonal test of L9 (3^4), and optimal process parameters are shown in Table 3.

ISSN: 2414-1895 DOI: 10.6919/ICJE.202605_12(5).0014

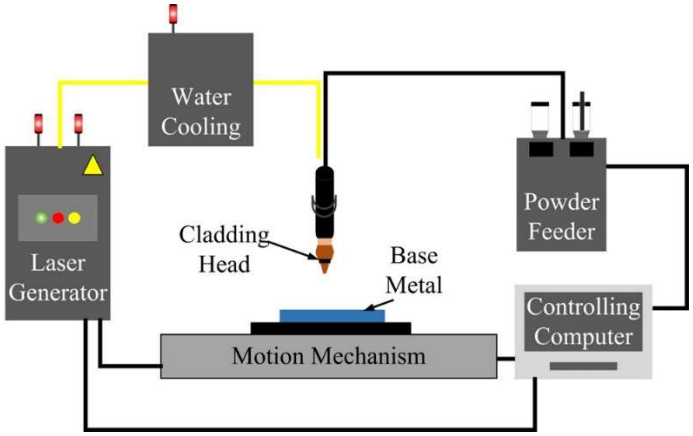

Figure 3. Schematic diagram of laser cladding.

Table 3. Optimal process parameters for laser cladding.

Sample	Laser Power(W)	Scanning velocity(mm/min)	powder flow rate(g/min)
Al_0Ti_{15}	1900	280	8.6
Al_5Ti_{10}	1900	200	8.3
$Al_{10}Ti_5$	1900	200	7.8
$Al_{15}Ti_0$	1900	200	7.6

2.2 Microstructure Characterization

The cross-section and surface of the metallographic specimen are polished. The samples were then corroded with a corrosive agent(volume ratio HCl: HNO_3 = 3:1) for 15 s. The cross-sectional microstructure and abrasion characteristics of $Fe_{20}Co_{20}Cr_{20}Ni_{25}Al_xTi_{(15-x)}$ high entropy alloy coatings were observed under an optical microscope (OM, OLYMPUSBX51), a scanning electron microscope (SEM, ZEISS Gemini 300) equipped with energy-dispersive X-ray spectroscopy (EDS). Besides, the cross-sectional microstructures are also characterized by electron Back Scatter Diffraction (EBSD, FEI QUANTAFEG250). The composition of the polishing coating was identified using an X-ray diffraction instrument (XRD, Bruker D8 Advanced). The parameters were set as follows: tube voltage 40 kV, tube current 30 mA, copper target, scanning speed 4°/min, scanning range 20-100°.

2.3 Mechanical Properties

The surface of the metallographic specimens was subjected to microhardness testing. The load during the test was 500 g and the holding time was 15 s.The test direction is perpendicular to the surface direction of the clad layer starting from the near surface of the clad layer, and the test points are spaced 0.10 mm apart, and the test points are distributed along the cladding layer, heat-affected zone and substrate direction in turn.

The maximum temperature of brake discs of high-speed trains with speeds above 400 km/h can reach 800 °C during braking. The ball and disc type high-temperature friction test machine (HT-1000) was used to conduct dry friction wear on coatings at room temperature (RT) and 800 °C. Figure 4 shows the schematic diagram. The friction disc with Φ30 mm and surface roughness Ra0.25 was cut on the coating layer, and the friction surface was polished smooth by using 80#, 180#, 400#, 600# and 1000# sandpaper in turn previously, and then ultrasonically cleaned by alcohol for 1 h. The material of the friction ball was copper-based powder metallurgical material of a high-speed train brake piece with a diameter of Φ6 mm, which satisfied TJ\ CL307-2019, the chemical composition is shown in Table

ISSN: 2414-1895 DOI: 10.6919/ICJE.202605_12(5).0014

4. Loading force is 15N, speed is 400 rpm and time is 90min. The experiment was performed twice at the same temperature to ensure the accuracy of the data. After 30 min of ultrasonic cleaning with alcohol, the wear rate was obtained using laser scanning confocal microscopy.

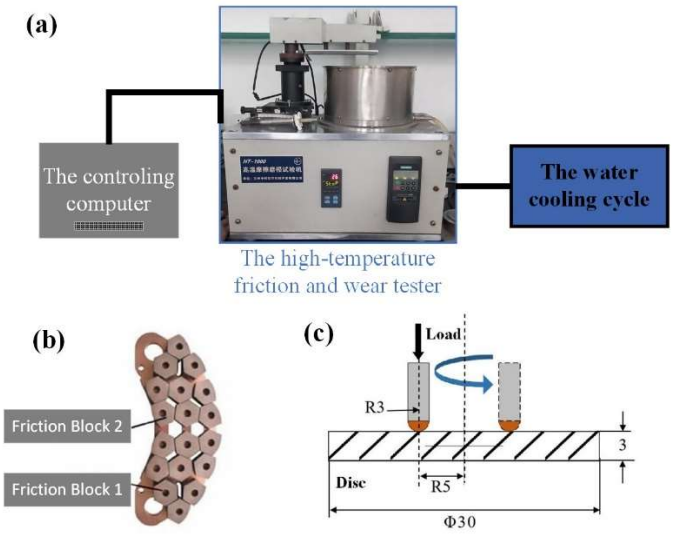

Figure 4. (a) Equipment diagram; (b) Copper-based gaskets; (c) The dimensions of the friction disc.

Table 4. The main chemical composition of the grinding ball table(wt.%).

Element	C	S	Cr	O	Cu	Fe
Ball	52.40	1.04	3.02	3.69	26.01	13.84

3. Results

3.1 Microstructure

Figure 5 shows the XRD pattern of the high-entropy coating. Figure 5 can be observed in the classical FCC structure with five typical peaks including (111), (200), (220), (311) and (222). Besides, the (111) peak intensity is the largest in the XRD pattern, which indicates that the high-entropy alloy coating is an FCC+BCC solid solution with a selective orientation in the (111) direction.

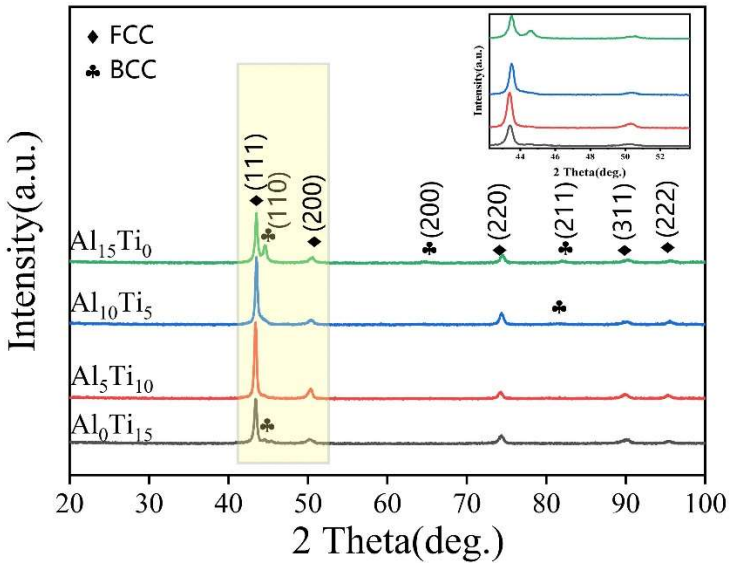

Figure 5. XRD patterns of the high-entropy coating.

ISSN: 2414-1895 DOI: 10.6919/ICJE.202605_12(5).0014

Figure 6 (a) to (d) shows the microstructure of the bottom of the $Fe_{20}Co_{20}Cr_{20}Ni_{25}Al_xTi_{(15-x)}$ high-entropy alloy coating and Figure 6 (e) to (h) show the enlarged areas of Figure 6 (a) to (d), respectively. The smooth plane crystals at the bonding interface between the heat-affected zone and the coating indicate that the substrate forms an effective metallurgical bond with the molten cladding layer [[29],[30]]. In addition, the microstructure of the bottom of the clad layer includes columnar crystals that are clearly parallel to the cooling direction, typical dendrite and intergranular structure. The columnar crystal of Al_0Ti_{15} is elongated, and the width of the columnar crystal increases with the increase of Al element and the decrease of Ti element. $Al_{10}Ti_5$ also distributes some bright white phases at the grain boundaries. The reason for the formation of intergranular regions is the different mixing enthalpy between the high-entropy alloy elements, and the mutual attraction and repulsion between the elements lead to the generation of composition subcooling regions during the laser melting process.

Figure 6 (i)~(l) show the microstructure of the top of the $Fe_{20}Co_{20}Cr_{20}Ni_{25}Al_xTi_{(15-x)}$ high-entropy alloy coating, and Figure 6 (m)~(p) shows the enlarged areas of Figure 6 (i)~(l), respectively. The microstructure of the coating is equiaxed crystal and intergranular microstructure. While the columnar crystals are growing, the top of the coating layer away from the melt pool has no preferential orientation in the central part of the melt pool due to the different heat flow direction, and the growth rate in the surrounding direction is equal, thus forming equiaxed crystals. In laser cladding, a protective gas cools and flows rapidly over the melt pool, removing heat. Therefore, the cooling rate in the top area of the melt pool is faster and the subcooling degree is larger, which eventually forms finer equiaxed crystals. As the addition of Ti element increases, it shows a gradual thinning of the equiaxial crystal, which is due to the larger atomic size of Ti element, which makes the diffusion ability of atoms much more difficult than the diffusion of other elements, reducing the driving force of interfacial migration and slowing down the growth of dendrites [[31]].

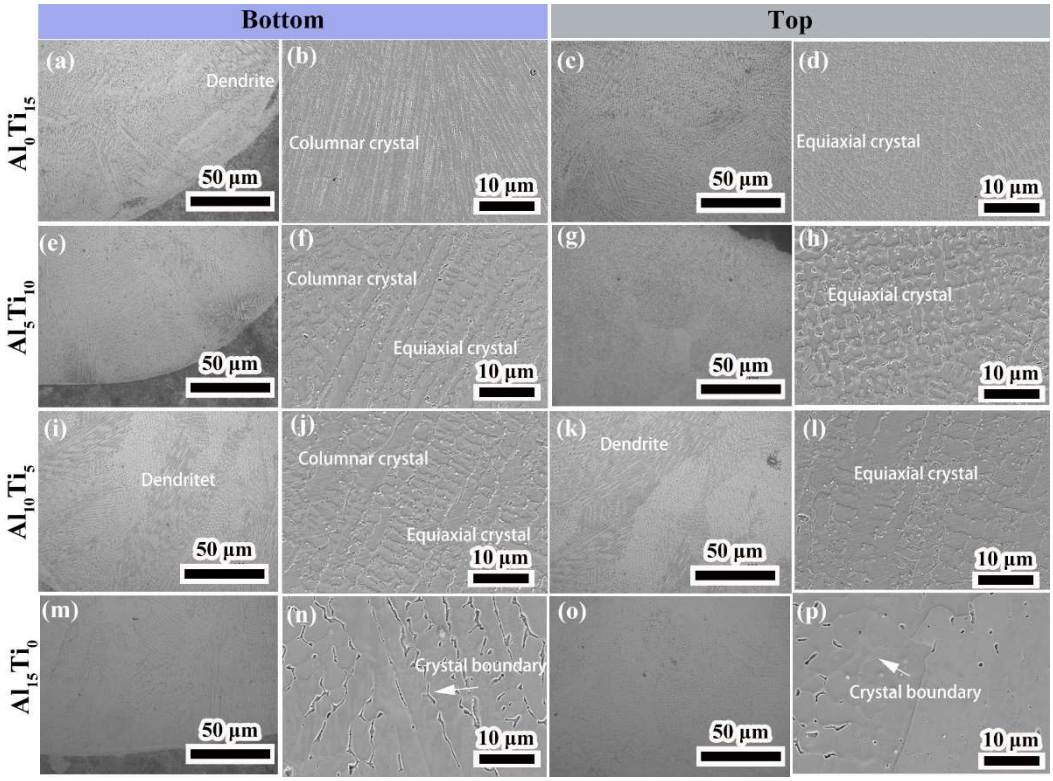

Figure 6. SEM morphology of high entropy alloy coating, (a)~(b) Al_0Ti_{15}; (c)~(d) Al_5Ti_{10}; (e)~(f) $Al_{10}Ti_5$; (g)~(h) $Al_{15}Ti_0$.

ISSN: 2414-1895 DOI: 10.6919/ICJE.202605_12(5).0014

Figure 7 shows the high magnification SEM images of the high entropy alloy coating. Bright white particles and irregular gray particles appear in the intercellular zone when the Ti content is not 0, and the white particle content decreases as the Ti content decreases. The laser melting process did not take place in a low oxygen environment, and the oxygen content in the environment around the melt pool, combined with the fast cooling and heating of laser melting and the convection effect of the melt pool, led to the high-temperature oxidation in the intercellular region, and the spherical white particles were mainly TiO_2 [[32]].

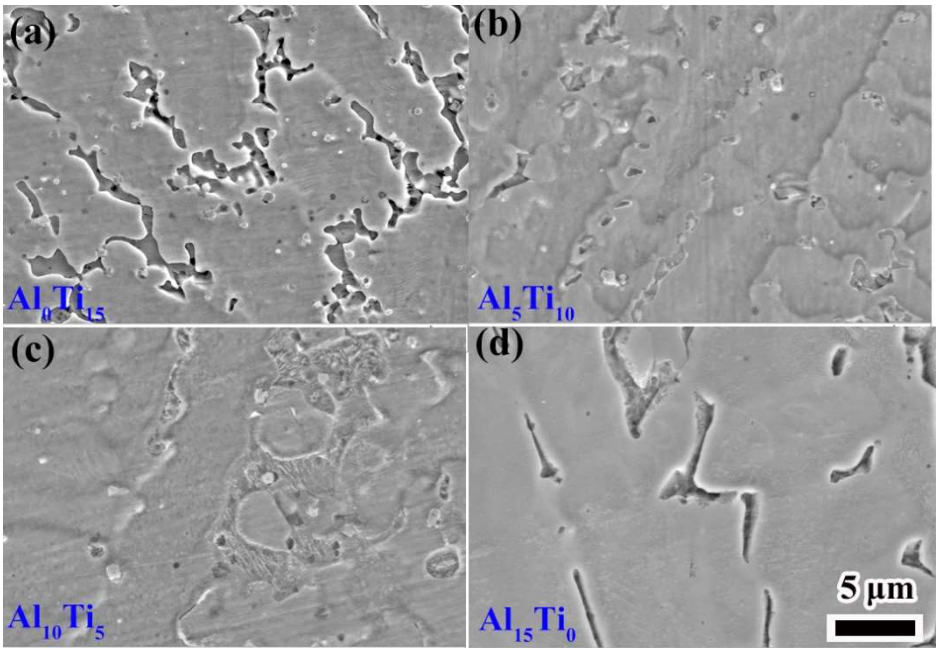

Figure 7. SEM morphology of high entropy alloy coating, (a) Al_0Ti_{15}; (b) Al_5Ti_{10}; (c) $Al_{10}Ti_5$; (d) $Al_{15}Ti_0$.

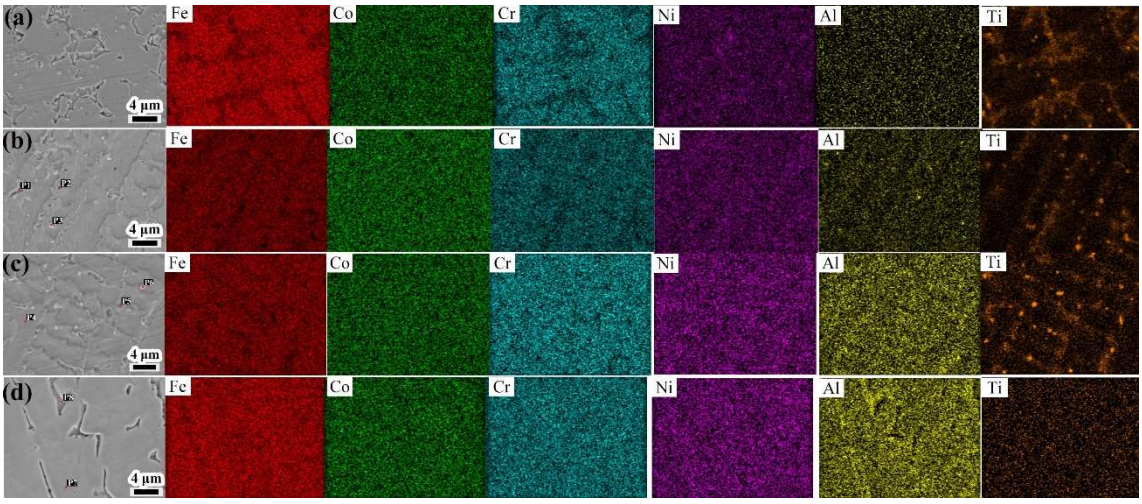

Figure 8. The chemical composition distribution maps of (a) Al_0Ti_{15}; (b) Al_5Ti_{10}; (c) $Al_{10}Ti_5$; (d) $Al_{15}Ti_0$.

To understand the elemental composition of the intercrystalline bright phase and intergranular dark phase of the $Fe_{20}Co_{20}Cr_{20}Ni_{25}Al_xTi_{(15-x)}$ high-entropy alloy coating, EDS was used to obtain Figure 8. The elements of Fe, Co, Cr, and Ni in the $Fe_{20}Co_{20}Cr_{20}Ni_{25}Al_xTi_{(15-x)}$ high-entropy alloy coating are uniformly distributed in the intercrystalline bright phase A (FCC). Ni and Ti are enriched in the intergranular dark phase B within the Al_0Ti_{15} high-entropy alloy coating, and the Ti elements are

ISSN: 2414-1895 DOI: 10.6919/ICJE.202605_12(5).0014

repelled by each other due to the large atomic size and the mixing enthalpy between Fe, Co and Cr is much larger than 0 kJ/mol, resulting in serious segregation. Al_5Ti_{10} high-entropy alloy coating is enriched in the intergranular Ti, and the Al elements are uniformly distributed within the crystal. $Al_{10}Ti_5$ and $Al_{15}Ti_0$ high entropy alloy coating is obviously enriched with Al in the intergranular area, and Al is more severely deviated compared with Ti.

Table 5 shows the total spectrum of the distribution diagram of $Fe_{20}Co_{20}Cr_{20}Ni_{25}Al_xTi_{(15-x)}$ high-entropy alloy. The actual Fe element content in the coating is higher than the theoretical content, which is mainly generated by the dilution of Fe elements in the matrix during the laser melting process, resulting in the actual content of Al and Ti elements in the coating being lower than the theoretical value.

Table 5. The total spectrum of the distribution diagram of $Fe_{20}Co_{20}Cr_{20}Ni_{25}Al_xTi_{(15-x)}$ high-entropy alloy(wt.%).

Sample	Fe	Co	Cr	Ni	Al	Ti
Al_0Ti_{15}	52.48	11.47	12.27	15.66	0.07	8.05
Al_5Ti_{10}	42.61	16.24	13.63	19.51	1.35	5.67
$Al_{10}Ti_5$	45.25	14.78	14.44	18.95	3.08	3.50
$Al_{15}Ti_0$	48.41	15.01	14.81	17.57	4.19	0.00

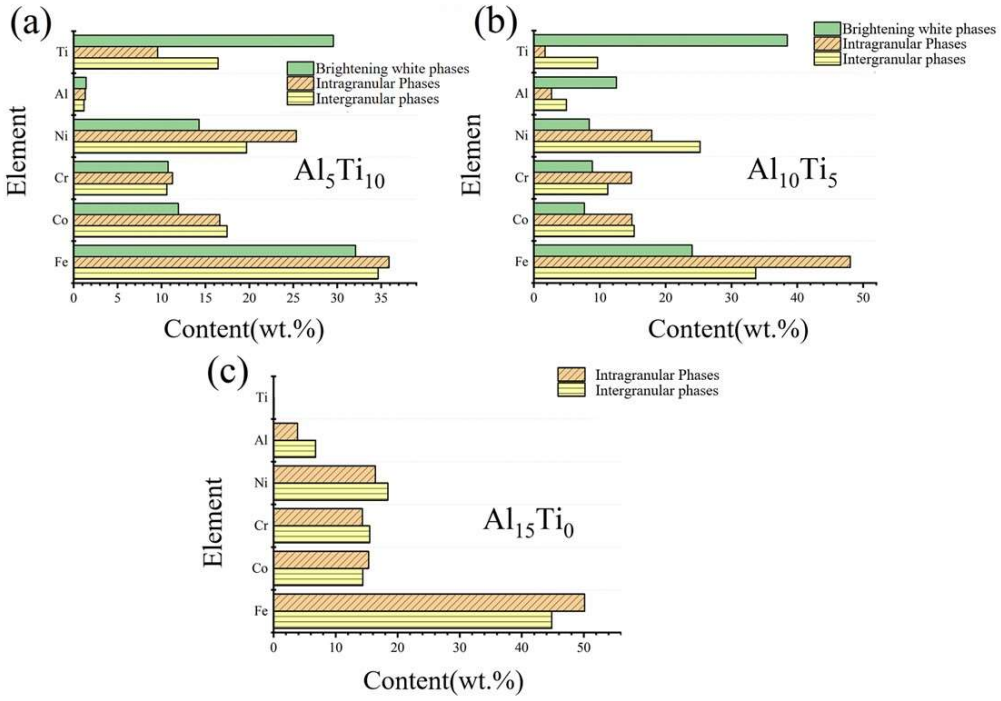

Figure 9. Distribution of intragranular, intergranular and bright white phase elements, (a) Al_0Ti_{15}; (b) Al_5Ti_{10}; (c) $Al_{10}Ti_5$; (d) $Al_{15}Ti_0$.

Figure 9 presents the results of point sweeping for various bright white phases in the Al_5Ti_{10} and $Al_{10}Ti_5$ high entropy alloy coatings. In the Al_5Ti_{10} coating, elements Ni, Co, and Ti are nearly equal in the intergranular P1 phase, while P2 contains twice as much Ti as Ni. Conversely, in the $Al_{10}Ti_5$

ISSN: 2414-1895 DOI: 10.6919/ICJE.202605_12(5).0014

coating, P4 is rich in Fe, Co, Cr, and Ni, and P5 has equal amounts of Ni and Ti. The bright white phase P6 is rich in Ti and Al elements, and the Ti/Al ratio is about 3:1. The $Al_{15}Ti_0$ high-entropy alloy coating Fe, Co, Cr, and Ni elements are uniformly distributed in the intercrystalline P7 and intergranular P8, and the intergranular is rich in Al elements. According to the point sweep results, the intercrystalline bright phase is the FCC phase rich in Fe, Co, Cr, and Ni.

To better define the phase composition and distribution and structural characteristics of the high-entropy alloy coatings, EBSD tests were conducted on four high-entropy alloy coating cross-sections, and the results are shown in **Figure 10**. From the GB diagram, the phases of $Al_{10}Ti_5$ tend to be equiaxed and the grain size is significantly smaller than that of the remaining three high-entropy alloy coatings, and the grains are mainly columnar in shape. The columnar grains mainly grow in the direction of coating construction, i.e. RD direction. The grain orientation relationship from the inverse polar map (IPF map) parallel to the RD direction reveals that the $Al_{10}Ti_5$ high-entropy alloy coating has the smallest grain orientation difference and the plasticity of the coating is relatively good, while the Al_0Ti_{15} takes the largest orientation difference. In terms of the phase map, the BCC content increases with increasing Al content, but the difference appears in $Al_{10}Ti_5$, where the BCC content is only 0.21%, which is less than the 0.93% of Al_0Ti_{15}. The presence of a small amount of BCC phase in the EBSD test results is consistent with the aforementioned XRD results.

The polar density distribution of FCC phase particles of the high-entropy alloy coatings is represented by polar plots (PFs) and inverse polar plots (IPFs). In the PFs, it was found that all the FCC phase particles of the high-entropy alloy coatings have orientation characteristics in the [100] direction. The maximum polar densities of Al_0Ti_{15}, Al_5Ti_{10}, $Al_{10}Ti_5$, and $Al_{15}Ti_0$ were 9.27, 8.92, 8.62, and 18.74, respectively, and $Al_{15}Ti_0$ had the most weave. The FCC phases of all high-entropy alloy coatings have orientation characteristics in the [1 0 0] direction.

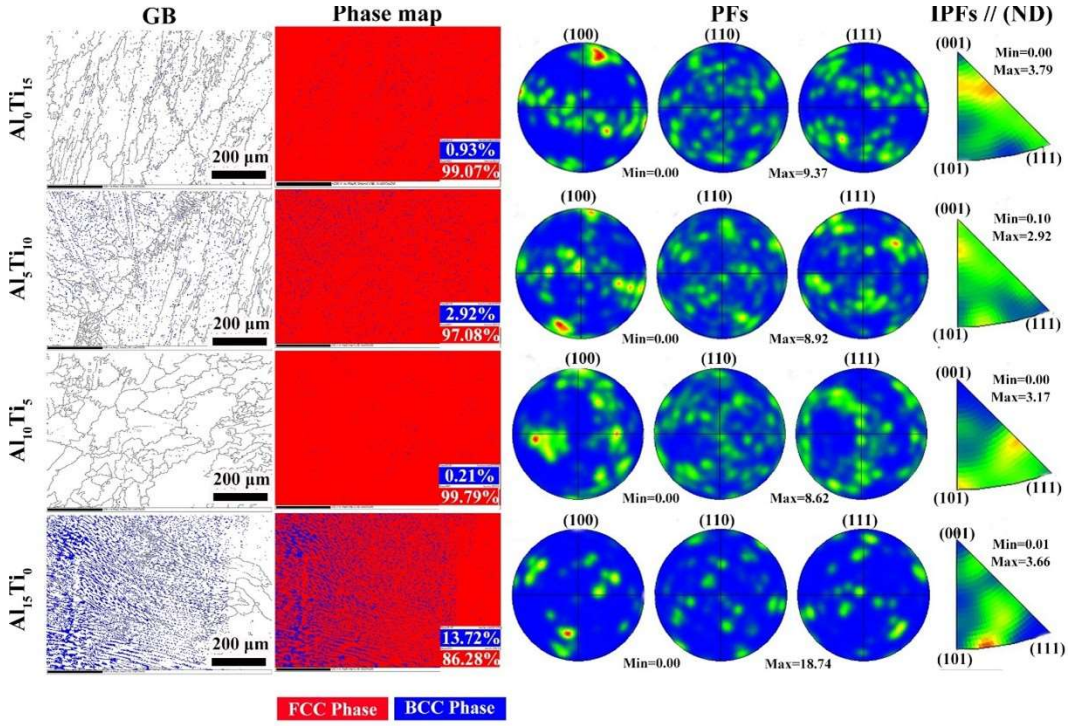

Figure 10. EBSD plot of the high entropy alloy coating.

3.2 Mechanical Properties

3.2.1 Microhardness

Figure 11 shows the microhardness of the coated HEAs. It is seen that the microhardness of the Al_0Ti_{15}, Al_5Ti_{10}, and $Al_{10}Ti_5$ coatings is not much different from that of the substrate, while the

ISSN: 2414-1895 DOI: 10.6919/ICJE.202605_12(5).0014

microhardness of the $Al_{15}Ti_0$ coating is smaller. The large atomic size of Ti element increases the effect of lattice distortion and increases the hardness and strength. The hardness of Al_5Ti_{10} is the largest. The microhardness of the high-entropy alloy coatings does not differ much from 24CrNiMo, meeting the requirements of the brake disc surface hardness. The heat-affected zone hardness reaches 600~700 $HV_{0.5}$, mainly because the laser also melts the substrate when melting the cladding layer, which experiences rapid cooling and heating, equivalent to quenching, and martensitic phase transformation occurs.

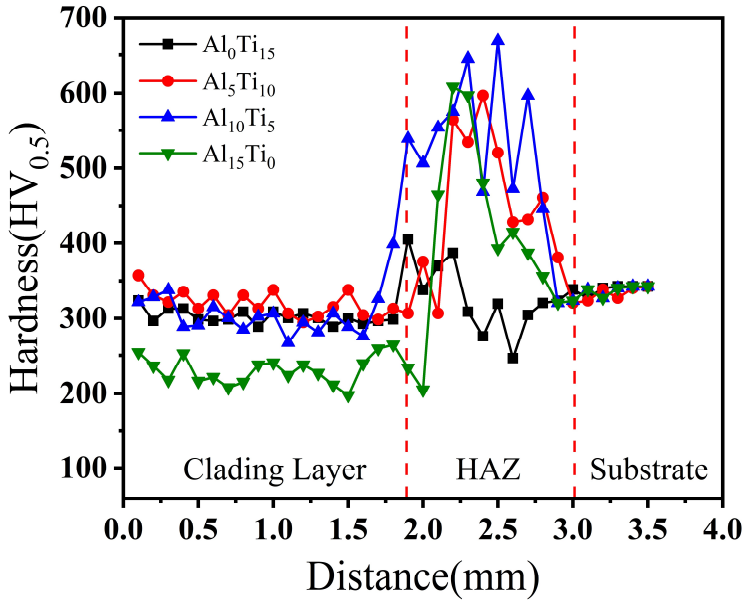

Figure 11. The microhardness of HEAs.

3.2.2 Friction Coefficient and Specific Wear Rate

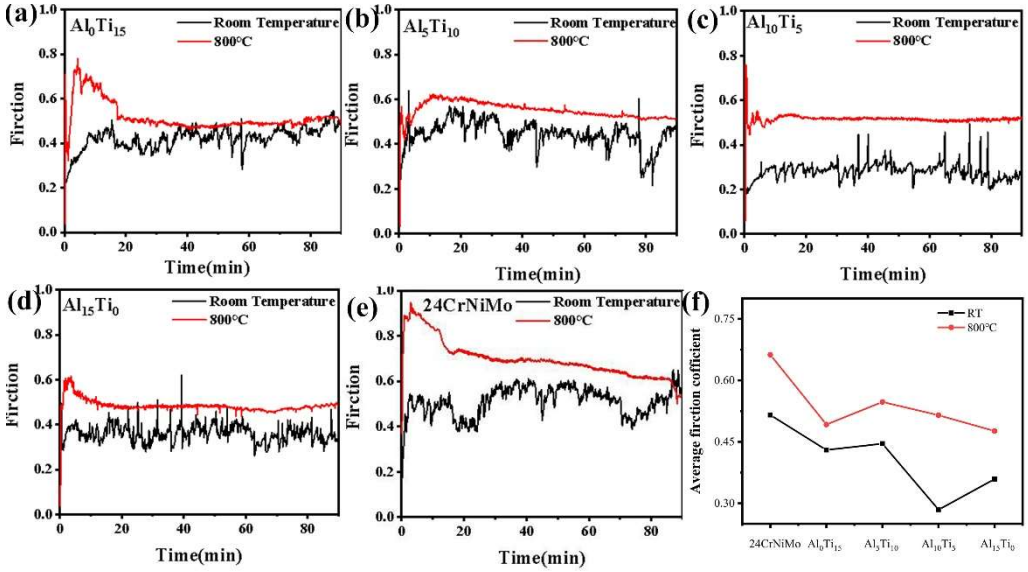

Figure 12. Friction coefficient (a) Al_0Ti_{15}; (b) Al_5Ti_{10}; (c) $Al_{10}Ti_5$; (d) $Al_{15}Ti_0$;(e)24CrNiMo; (f) average friction coefficient.

The friction coefficient reflects the magnitude of the contact stress between the friction pair. The higher the friction coefficient, the greater the contact stress between the friction pair. Therefore, the friction coefficient also indirectly reflects the lubrication condition of the contact area of the friction pair or the formation of the stable friction protection film. [[33],[34]]. Figure 12 shows that the contact surface is small at room temperature during the initial stage of wear, which leads to an unstable

ISSN: 2414-1895 DOI: 10.6919/ICJE.202605_12(5).0014

contact between the grinding ball and the coating layer, resulting in a rapid decline in the friction coefficient. The friction process stabilizes after 5~20 min, whilst the frictional coefficient gradually stabilizes. The friction coefficient of the high entropy alloy coatings at both room temperature and 800℃ are lower than those of the substrate. The stability of the friction coefficient of the high entropy alloy cladding layer at 800 ℃ is better than that of the substrate, which can meet the friction coefficient requirements and ensure the safety and reliability of braking when braking in high-speed trains.

The average friction coefficient of Al_0Ti_{15} at RT and 800 ℃ is not much different, and the average friction coefficient of Al_5Ti_{10}, $Al_{10}Ti_5$ and $Al_{15}Ti_0$ at 800 ℃ increases compared to RT. Among these, the average friction coefficient at 800 ℃ of $Al_{10}Ti_5$ increased by nearly 50% compared to RT. The reason may be that the roughness of the friction surface is very different at room temperature and 800 °C, or it may be that the properties of the friction disc or friction sub-material are affected at 800 °C [[35]].

Figure 13 shows the wear rate and the abrasion cross-sectional track. At 800 ℃, the average wear rate of the high-entropy alloys was all in the range of 9×10^{-5}~14×10^{-5} $mm^3\cdot(m\cdot min)^{-1}$. The average wear rates of Al_0Ti_{15}, Al_5Ti_{10}, $Al_{10}Ti_5$ and $Al_{15}Ti_0$ were 77.2%, 74.2%, 83.0% and 75.9% lower than those of the substrate, respectively. The results showed positive correlation between hardness and wear resistance. In general, the room temperature and high-temperature wear of Al_0Ti_{15}, Al_5Ti_{10} and $Al_{10}Ti_5$ high entropy alloy coatings are better than the substrate. Figure 13 (b) and (c) show the abrasion cross-sectional track. The width and depth of the wear traces at RT of the substrate are 1809.0 μm and 32.3 μm, respectively. With the increase the content of Al element, the abrasion width increases, and it is 982.6 μm, 1640.2 μm, 1749.0 μm and 2484.8 μm, respectively. The width and depth of the abrasion at RT of Al_0Ti_{15}, Al_5Ti_{10} and $Al_{10}Ti_5$ are smaller than those of the substrate. The width and depth of the abrasion of the substrate at 800 ℃ are 2662.6 μm and 25.4 μm, respectively. The abrasion widths of Al_5Ti_{10}, $Al_{10}Ti_5$ and $Al_{15}Ti_0$ are 2411.2 μm, 2383.6 μm, 2133.3 μm and 3226.6 μm respectively, which are reduced by 9.44%, 10.48%, 19.88% and -21.18%, respectively, compared with the substrate. The irregular bulge at the edge part of the abrasion profile at high temperature is thought to be the improved toughness of the HEAs in a high-temperature environment and the plastic deformation due to extrusion.

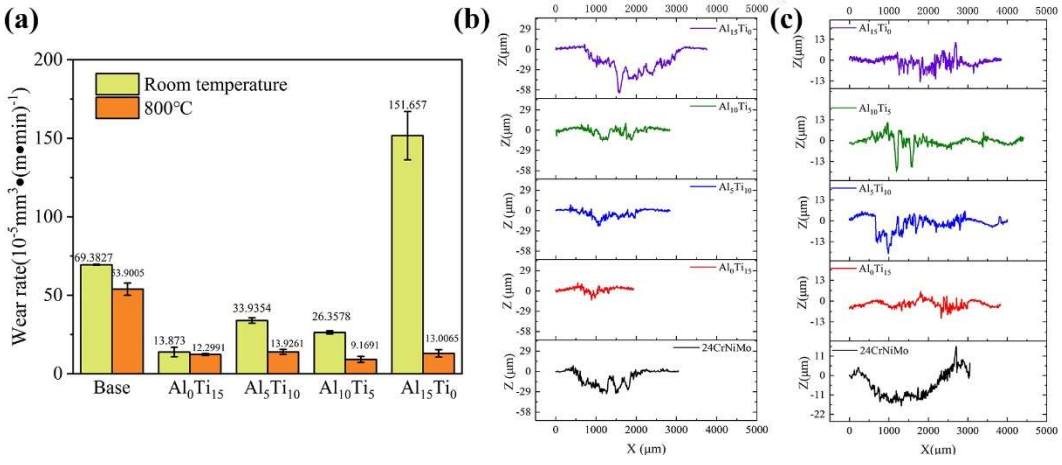

Figure 13. (a)wear rate; (b) cross-sectional abrasion track at RT; (c) abrasion track at 800 ℃.

3.2.3 Worn Surface and Wear Mechanism

Figure 14 shows the SEM of frictional wear characteristics of the substrate and the high-entropy alloy coatings at RT and 800 °C. The variation of wear morphology can explain the process of its wear amount variation. The substrate and the Al_5Ti_{10} and $Al_{10}Ti_5$ high-entropy alloy coatings have obvious adhesion layers in addition to the grooves and debris. The frictional heat generated by friction disc and friction against the grinding ball causes a small amount of oxide at the abrasion and even a dark

ISSN: 2414-1895 DOI: 10.6919/ICJE.202605_12(5).0014

oxide layer, oxidative wear occurs. The main wear mechanism of the substrate and Al_5Ti_{10} and $Al_{10}Ti_5$ high-entropy alloy coatings is a mixed wear mechanism with mainly abrasive wear and supplemented by adhesive wear and oxidation wear. The wear surface characteristics of Al_0Ti_{15} and $Al_{15}Ti_0$ high-entropy alloy coatings are obvious grooves, debris, and little dark oxide layer, which indicate their wear as a mixture of abrasive wear and oxidative wear. The shallow furrows of Al_0Ti_{15} compared to those of $Al_{15}Ti_0$ are thought to be due to the former's greater hardness [[36],[37]].

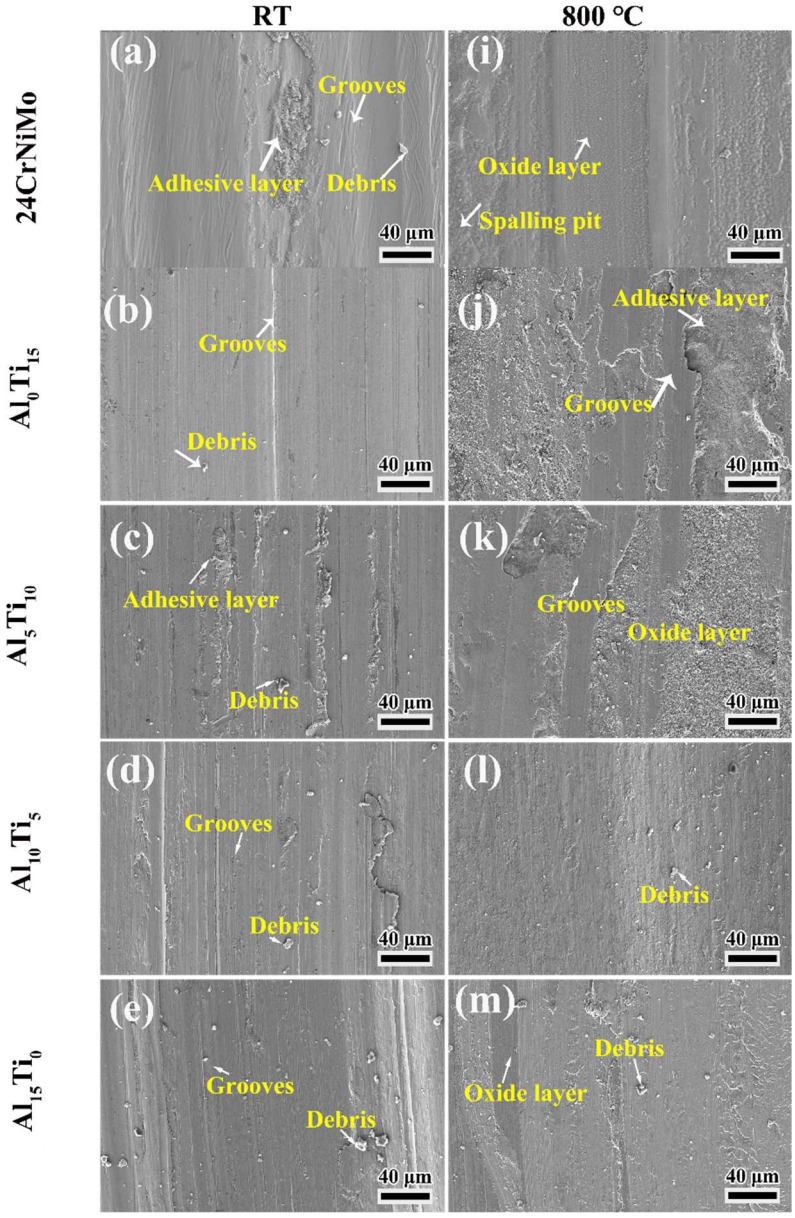

Figure 14. SEM morphology of frictional wear characteristics.

At 800°C, a certain degree of oxidation reaction occurs in both the substrate material and the high entropy alloy coating, and the grinding balls rub in direct contact with the generated oxides. Due to the different compositions of their oxides, there are differences in the morphology after wear. Significant material spalling and debris accumulation on the surface of the wear marks indicate that severe adhesive wear occurs during the friction process, which also leads to fluctuations in friction coefficient. When the accumulation of metal abrasive chips to a certain extent occurs extrusion and oxidation, the surface of the high entropy alloy coating layer will form oxide films with wear reducing effect, and these oxide films are in direct contact with the copper-based gates to participate in the

ISSN: 2414-1895 DOI: 10.6919/ICJE.202605_12(5).0014

frictional wear behavior, which to some extent reduces the wear of the HEAs and stabilizes the friction coefficient. At 800 ℃, the elements in the high entropy alloy produce oxides, which are crushed and broken or even fall off the oxide debris produced by the grinding surface roughness increases, and the friction coefficient is increased.

To clarify the high-temperature frictional wear mechanism, the wear surfaces were examined for composition and physical phase. In terms of macroscopic property changes, the strength of the copper-based material on the friction ball decreases significantly at 800 °C [[38]], which leads to a remarkable reduction in the resistance to plastic deformation. Moreover, the strength of the high-entropy alloy-coated friction disc is stronger than that of the copper-based gate material (33.4 HB), which also leads to the transfer of copper-based material to the friction disc surface during high-temperature friction. Migration of unusually active Cu atoms from the docking ball to the wear surface at high temperatures, which is typical of adhesive wear. It is worth mentioning that the content and distribution of Cu elements on the wear surface can indicate the degree of adhesive wear. From the distribution of Cu elements in the EDS of Figure 15, it can be obtained that the degree of adhesive wear is Al_5Ti_{10}, Al_0Ti_{15}, $Al_{15}Ti_0$, 24CrNiMo, and $Al_{10}Ti_5$ from the content of O elements, the degree of oxidative wear is 24CrNiMo, Al_0Ti_{15}, $Al_{10}Ti_5$, Al_5Ti_{10}, and $Al_{15}Ti_0$ from the highest to the lowest. The substrate and the high-entropy alloy coating produce a large amount of Fe_3O_2 at 800°C. High entropy alloy coating wear surface oxides are Fe_3O_2, TiO_2, Cr_3O_2 and a small amount of Al_3O_2 [[39]]. The actual content of elemental Al and Fe is lower than the theoretical content because the Al_3O_2 and Fe_3O_2 oxide films are continuously destroyed under high-temperature wear, resulting in partial loss. The elemental content of Cu in the grinding surface area is high, and the adhesive wear is serious.

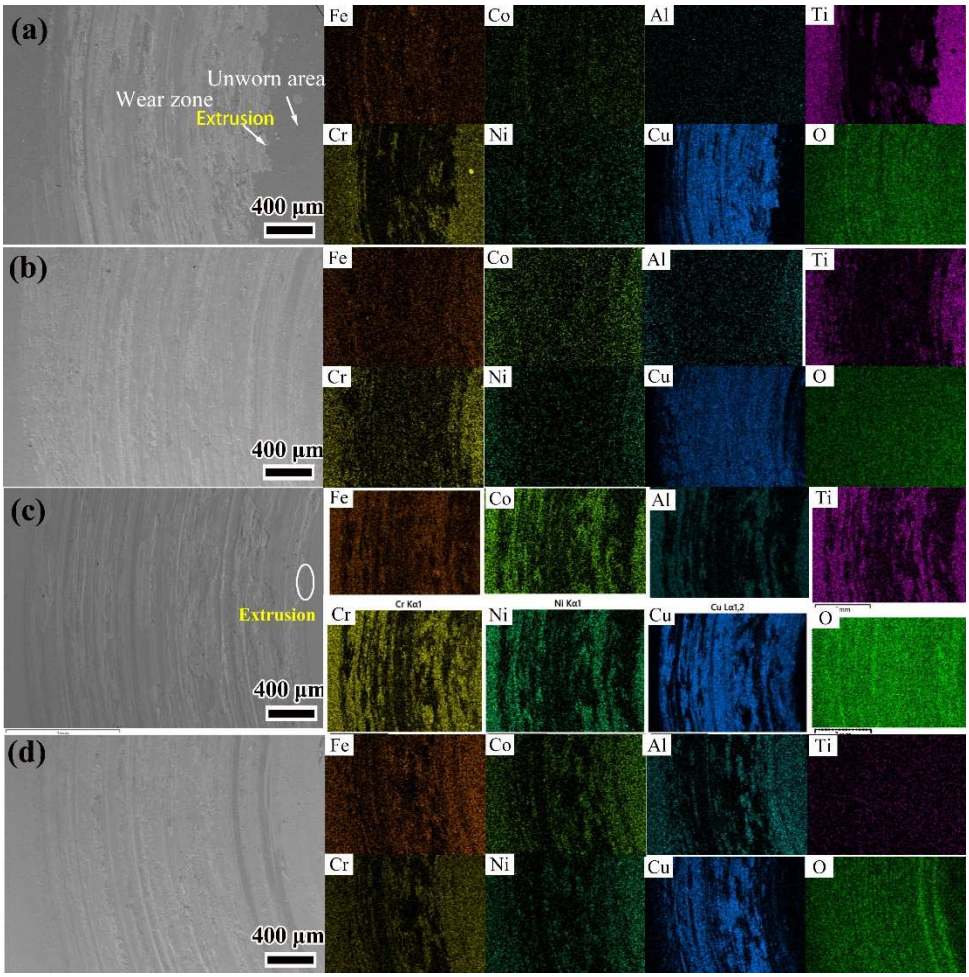

Figure 15. The chemical composition distribution maps of wear trace at 800 ℃ (a) Al_0Ti_{15}; (b) Al_5Ti_{10}; (c) $Al_{10}Ti_5$; (d) $Al_{15}Ti_0$.

ISSN: 2414-1895 DOI: 10.6919/ICJE.202605_12(5).0014

Figure 16 shows schematic diagram of the wear process of HEAs at 800 ℃. The wear mechanism of Al_0Ti_{15} and $Al_{15}Ti_0$ changed from abrasive wear to oxidative wear and adhesive wear, and the wear mechanism of Al_5Ti_{10} and $Al_{10}Ti_5$ coatings changed to oxidative wear and abrasive wear.

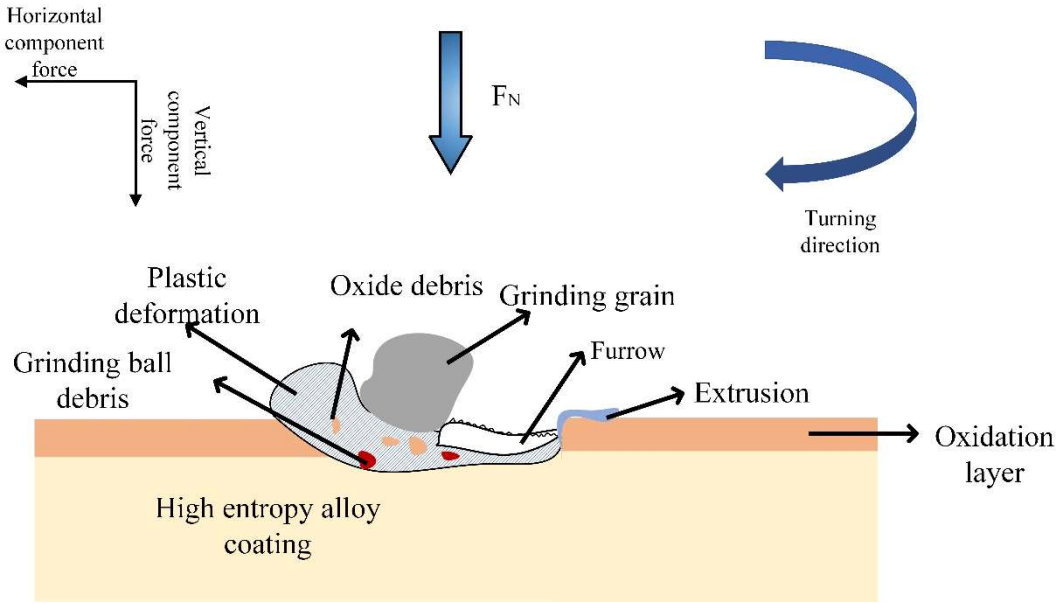

Figure 16. Schematic diagram of the wear process of high entropy alloys at 800 ℃.

4. Conclusion

In the paper, defect-free $Fe_{20}Co_{20}Cr_{20}Ni_{25}Al_xTi_{(15-x)}$ high entropy alloy high-performance coatings were prepared by laser cladding and the effects of Al and Ti elements on microstructure, micro-hardness and high-temperature friction wear properties and mechanism were investigated. The following conclusions can be drawn:

(1) The $Fe_{20}Co_{20}Cr_{20}Ni_{25}Al_xTi_{(15-x)}$ high-entropy alloy coating can form a stable FCC+BCC mixed solid solution. The microstructure of the clad layer from bottom to top is plane crystal, columnar crystal, dendritic crystal and equiaxial crystal, respectively.

(2) The hardness of Al_0Ti_{15}, Al_5Ti_{10} and $Al_{10}Ti_5$ clad layers are all around 300~350 HV0.5, and $Al_{15}Ti_0$ has the highest hardness. The friction coefficients of the high-entropy alloy molten cladding layers at room temperature and 800 ℃ are all in the range of 0.3~0.6, which are lower than those of the substrate. The room temperature wear rates of Al_0Ti_{15}, Al_5Ti_{10}, $Al_{10}Ti_5$, and $Al_{15}Ti_0$ are reduced by 80.0%, 51.1%, 62.0% and -118.2%, respectively, compared with those of the substrate. at 800 ℃. The wear rates of Al_0Ti_{15}, Al_5Ti_{10}, $Al_{10}Ti_5$, and $Al_{15}Ti_0$ high entropy alloys were reduced by 77.2%, 74.2%, 83.0% and 75.9%, respectively, compared to the substrate. The hardness and strength of HEAs were positively correlated with wear. In general, the room temperature and high-temperature wear of Al_0Ti_{15}, Al_5Ti_{10}, and $Al_{10}Ti_5$ high-entropy alloy coatings were better than the substrate. Room-temperature friction wear is dominated by abrasive wear, and high-temperature friction wear is a mixture of oxidation wear, abrasive wear and adhesive wear.

Acknowledgments

This research received no external funding.

References

[1] Xiao, Y.; Zhang, Z.; Yao, P.; Fan, K.; Zhou, H.; Gong, T.; Zhao, L.; Deng, M. Mechanical and Tribological Behaviors of Copper Metal Matrix Composites for Brake Pads Used in High-Speed Trains. Tribology International 2018, 119, 585–592.

ISSN: 2414-1895 DOI: 10.6919/ICJE.202605_12(5).0014

[2] Lu, C.; Ren, Z.; Ma, C. Study on the Technologies Development Trend of High Speed EMUs. High-speed Railway 2023, 1, 1–5.

[3] Yoo, J.J.; Byun, K.S. Development of Sensor for the Real-Time Monitoring of Brake Pad Wear and Brake Disc Temperature in High Temperature. International Journal of Automotive Technology 2023, 24, 1603–1613, doi:10.1007/s12239-023-0129-z.

[4] Xie, X.; Li, Z.; Domblesky, J.P.; Yang, Z.; Liu, X.; Li, W.; Han, J. Analysis of Deep Crack Formation and Propagation in Railway Brake Discs. Engineering Failure Analysis 2021, 128, 105600, doi:10.1016/j.engfailanal.2021.105600.

[5] Zhu, H.; Lian, S.; Jin, M.; Wang, Y.; Yang, S.; Lu, Q.; Tao, Z.; Xiao, Q. Review of Research on the Influence of Vibration and Thermal Fatigue Crack of Brake Disc on Rail Vehicles. Engineering Failure Analysis 2023, 153, 107603, doi:10.1016/j.engfailanal.2023.107603.

[6] Zhao, Y.; Chen, H. Strength-Toughness Design and Braking Behavior Study of Coatings for 400 Km/H High-Speed Train Brake Discs; Elsevier BV, 2025.

[7] Wu, Y.; Zou, G.; Liu, Y.; A, Z.; Zhao, W.; Wang, W.; Xue, J.; Zhang, Y.; Jia, Q.; Chen, H. Temperature Dependence of the Tensile and Thermal Fatigue Cracking Properties of Laser-Deposited Cobalt-Based Coatings for Brake Disc Application. SSRN Electronic Journal 2022, doi:10.2139/ssrn.4177903.

[8] Shi, X.; Wen, D.; Wang, S.; Wang, G.; Zhang, M.; Li, J.; Xue, C. Investigation on Friction and Wear Performance of Laser Cladding Ni-Based Alloy Coating on Brake Disc. Optik 2021, 242, 167227, doi:10.1016/j.ijleo.2021.167227. Hu, H.

[9] Tang, G.; Cheng, Z.; Pan, Y.; Huang, Z.; Ding, W.; Liang, Z. Co-Cr3c2 Coating Incorporating Grain Refinement and Dislocation Density Gradient to Enhance Wear Resistance of 24crnimo Steel; Elsevier BV, 2024;

[10] Yeh, J. w.; Chen, S. k.; Lin, S. j.; Gan, J. y.; Chin, T. s.; Shun, T. t.; Tsau, C. h.; Chang, S. y. Nanostructured High-Entropy Alloys with Multiple Principal Elements: Novel Alloy Design Concepts and Outcomes. Advanced Engineering Materials 2004, 6, 299–30.

[11] Cantor, B.; Chang, I.T.H.; Knight, P.; Vincent, A.J.B. Microstructural Development in Equiatomic Multicomponent Alloys[J]. Materials Science and Engineering: A 2004, 375–377, 213–218.

[12] Wu, H.; Zhang, S.; Wu, C.L.; Zhang, C.H.; Sun, X.Y.; Bai, X.L. Electrochemical Corrosion Behavior in Sulfuric Acid Solution and Dry Sliding Friction and Wear Properties of Laser-Cladded CoCrFeNiNb High Entropy Alloy Coatings[J]. Surface and Coatings Technology 2023, 460, 12942.

[13] Lu, Y.; Peng, Y.; Chang, X.; Xiu, W.; Shi, Z. Insights on Microstructure and Tribological Properties of FeCoCrNiMo HEA Reinforced CuSn Coatings by Laser Cladding for Monorail Brakes. Wear 2025, 580–581, 206244, doi:10.1016/j.wear.2025.206244.

[14] Huang, Z.; Lu, X.; Yan, M.; Fu, Y. Evaluating stability, elastic and thermodynamic properties of AlTiNiCuCox (x = 0.5,0.75,1,1.25,1.5) high entropy alloys[J]. Materials Research Express 2019, 6(12), 126581. doi:10.1088/2053-1591/ab48a8.

[15] Praveen S, Kim H S. High-Entropy Alloys: Potential Candidates for High-Temperature Applications – An Overview[J]. Advanced Engineering Materials, 2018, 20.

[16] Dewangan, S.K.; Mangish, A.; Kumar, S.; Sharma, A.; Ahn, B.; Kumar, V. A Review on High-Temperature Applicability: A Milestone for High Entropy Alloys[J]. Engineering Science and Technology, an International Journal 2022, 35.

[17] Miracle D B, Senkov O N. A critical review of high entropy alloys and related concepts[J]. Acta Materialia, 2017, 122: 448-511.

[18] George E P, Curtin W A, Tasan C C. High entropy alloys: A focused review of mechanical properties and deformation mechanisms[J]. Acta Materialia, 2020, 188: 435-474.

[19] Wang, Z. G.; Zhou, W.; Fu, L. M.; Wang, J. F.; Luo, R. C.; Han, X. C.; et al. Effect of coherent L12 nanoprecipitates on the tensile behavior of a fcc-based high-entropy alloy[J]. Materials Science and Engineering: A 2017, 696, 503–510.

[20] Ding, Z. Y.; Cao, B. X.; Luan, J. H.; Jiao, Z. B. Synergistic effects of Al and Ti on the oxidation behaviour and mechanical properties of L12-strengthened FeCoCrNi high-entropy alloys[J]. Corrosion Science 2021, 184, 109365.

ISSN: 2414-1895 DOI: 10.6919/ICJE.202605_12(5).0014

[21] He, J.Y.; Wang, H.; Huang, H.L.; Xu, X.D.; Chen, M.W.; Wu, Y.; Liu, X.J.; Nieh, T.G.; An, K.; Lu, Z.P. A Precipitation-Hardened High-Entropy Alloy with Outstanding Tensile Properties[J]. Acta Materialia 2016, 102, 187–196.

[22] Yang, Y.-C.; Liu, C.; Lin, C.-Y.; Xia, Z. The Effect of Local Atomic Configuration in High-Entropy Alloys on the Dislocation Behaviors and Mechanical Properties[J]. Materials Science and Engineering: A 2021, 815, 141253.

[23] Xu, H.; Zhang, M.; Zhang, G.; Li, G.; Li, G. Microstructure and Mechanical Property of Al,Ti Co-Adding L21-Strengthened NiCrFe-Based HEAs[J]. Materials Characterization 2024, 207, 113516.

[24] Guo, Y.; Yang, F.; Lu, B.; Qiu, H.; Zhu, J.; Wang, D.; Yan, X.; Qiu, Z.; Yin, S.; Liu, M. Competitive Relationship between the FCC + BCC Dual Phases in the Wear Mechanism of Laser Cladding FeCoCrNiAl0.5Ti0.5 HEAs Coating[J]. Surface and Coatings Technology 2024, 493, 131315.

[25] Garrido, B.; Dosta, S.; Cano, I.G. Bioactive Glass Coatings Obtained by Thermal Spray: Current Status and Future Challenges[J]. Boletín de la Sociedad Española de Cerámica y Vidrio 2022, 61, 516–530.

[26] Yang, W.; Chen, G.; Wang, P.; Qiao, J.; Hu, F.; Liu, S.; Zhang, Q.; Hussain, M.; Dong, R.; Wu, G. Enhanced Thermal Conductivity in Diamond/Aluminum Composites with Tungsten Coatings on Diamond Particles Prepared by Magnetron Sputtering Method[J]. Journal of Alloys and Compounds 2017, 726, 623–631.

[27] Arif, Z.U.; Khalid, M.Y.; ur Rehman, E.; Ullah, S.; Atif, M.; Tariq, A. A Review on Laser Cladding of High-Entropy Alloys, Their Recent Trends and Potential Applications[J]. Journal of Manufacturing Processes 2021, 68, 225–273.

[28] Das, A.K. A Review on Coating with High Entropy Alloy Developed by Laser Energy Based Surfacing Process[J]. Materials Today: Proceedings 2022, 52, 1551–1557.

[29] Wang, J.; Chen, Y.; Zhang, Y.; Dai, W.; Xu, Q.; Li, W.; Liu, Y. Corrosion and Slurry Erosion Wear Performances of Coaxial Direct Laser Deposited CoCrFeNiCu1-xMox High-Entropy Coatings by Modulating the Second-Phase Precipitation[J]. Materials & Design 2021, 212, 110277.

[30] Yang, J.; Bai, B.; Ke, H.; Cui, Z.; Liu, Z.; Zhou, Z.; Xu, H.; Xiao, J.; Liu, Q.; Li, H. Effect of Metallurgical Behavior on Microstructure and Properties of FeCrMoMn Coatings Prepared by High-Speed Laser Cladding. Optics & Laser Technology 2021, 144, 107431.

[31] Zhang J B, Li X, Zhang Y C, et al. Sluggish dendrite growth in an undercooled high entropy alloy[J]. Intermetallics, 2020, 119: 106714.

[32] Wang, J.; Chen, Y.; Zhang, Y.; Zhang, Y.; Li, J.; Liu, J.; Liu, Y.; Li, W. Microstructure evolution and acid corrosion behavior of CoCrFeNiCu1−xMox high-entropy alloy coatings fabricated by coaxial direct laser deposition[J]. Corrosion Science, 2022, 198: 110108.

[33] Wu, T.; Yang, C.; Yu, L.; Zheng, X.; Zhang, L.; Jiang, Y.; Xue, Y.; Lu, Y.; Luan, B. Microstructure Characterization and High-Temperature Wear Mechanism of High-Entropy Alloy Matrix Composite Coating Fabricated by Laser Cladding. Applied Surface Science 2024, 677, 161032, doi:10.1016/j.apsusc.2024.161032.

[34] Yu, D.T.; Wu, C.L.; Cui, X.X.; Zhao, X.B.; Zhang, S.; Zhang, C.H. Study on Microstructure, Mechanical Properties, Wear and Cavitation Erosion Resistance of FeCrNiTi0.3Al0.3 High Entropy Alloy Coatings by Laser Cladding[J]. Materials Today Communications 2025, 49, 113840.

[35] Lu, C.; Jiang, X.; Chen, X.; Mo, J. Experimental study on the evolution of friction and wear behaviours of railway friction block during temperature rise under extreme braking conditions[J]. Engineering Failure Analysis, 2022, 141: 106621.

[36] Nguyen, C.; Tieu, A.K.; Deng, G.; Wexler, D.; Tran, B.; Vo, T.D. Study of Wear and Friction Properties of a Co-Free CrFeNiAl0.4Ti0.2 High Entropy Alloy from 600 to 950 °C. Tribology International 2022, 169, 107453.

[37] Liang, C.; Wang, C.; Zhang, K.; Tan, H.; Liang, M.; Xie, Y.; Liu, W.; Yang, J.; Zhou, S. Mechanical and Tribological Properties of (FeCoNi)88-x(AlTi)12Mox High-Entropy Alloys. International Journal of Refractory Metals and Hard Materials 2022, 105, 105845.

[38] Xiao, Y.; Cheng, Y.; Shen, M.; Yao, P.; Du, J.; Ji, D.; Zhao, H.; Liu, S.; Hua, L. Friction and Wear Behavior of Copper Metal Matrix Composites at Temperatures up to 800 °C. Journal of Materials Research and Technology 2022, 19, 2050–206.

ISSN: 2414-1895 DOI: 10.6919/ICJE.202605_12(5).0014

[39] Lin, G.; Cai, Z.; Dong, Y.; Wang, C.; Hu, J.; Zhang, P.; Gu, L. High-Temperature Oxidation Behavior of AlCoCrFeNi2.1 Eutectic High-Entropy Alloy: Microstructure Evolution and Microhardness. Materials Characterization 2024, 210, 113830.